RSC Advances

PAPER

View Article Online
View Journal | View Issue

Cite this: *RSC Adv.*, 2025, **15**, 4573

Enzymatic properties of iron oxide nanoclusters and their application as a colorimetric glucose detection probe†

Dahyun Bae, Minhee Kim and Jin-sil Choi *

Nanozymes have attracted attention owing to their distinct catalytic capabilities and potential applications, being advantageous compared to natural enzymes in terms of storage and cost efficiency. In this study, we investigated the enzymatic properties of iron oxide nanoclusters (IOCs) formed through the clustering of small nanoparticles. Our findings reveal that the enzymatic activity of IOCs is enhanced as their size increases. Additionally, we demonstrated that the size of the unit particles within IOCs is highly dependent on the nucleation environment, which is a crucial factor in determining the overall size of the IOCs. Importantly, the surface area of IOCs is more closely related to the size of the individual unit particles rather than the entire cluster. Smaller unit particle sizes within IOCs resulted in an increase in nanocluster size, thereby augmenting the specific surface area. The optimal IOC exhibited superior stability under various conditions and a broader range of reactivity compared to natural enzymes, making it a promising probe material for point-of-care tests across diverse environments. Furthermore, its effectiveness as a glucose detection probe was demonstrated, highlighting its potential for practical applications. The remarkable enzyme-like efficacy of IOCs not only enhances their utility in on-site detection technologies but also establishes them as a versatile detection probe.

Received 2nd January 2025
Accepted 27th January 2025

DOI: 10.1039/d5ra00047e

rsc.li/rsc-advances

Introduction

Nanozymes, a class of artificial enzymes based on nanoparticles, have emerged as promising alternatives for natural enzymes for various applications. Natural enzymes have been applied to sensor systems and chemical synthesis procedures owing to their remarkable catalytic efficiency and specificity,[1] however, they exhibit limitations such as low yield, expensive purification processes, and instability in diverse environments.[2] Nanomaterials offer a promising solution to these challenges owing to their distinctive physicochemical properties, robust functional characteristics, adjustable catalytic capabilities, precise structural compositions, resilience to harsh conditions, ease of modification, excellent stability, and suitability for large-scale production.[3–6] Based on this, the attention of researchers has been drawn to design optimal nanozymes for wide applications of nanozymes in various biological systems including sensing.[7] For example, metal–organic framework (MOF)-on-MOF nanozymes, which integrate multiple anisotropic MOFs into a single unit, offer increased active sites, thereby enhancing catalytic activity due to their heterogeneous components and diverse structures.[8–11] Consequently, MOF-on-MOF nanozymes present a novel signal amplification strategy for electrochemiluminescence bioassays, paving the way for practical clinical applications of MOFs in ultrasensitive immunoassays. Doping of metal into carbon nanostructure can improve their enzymatic activity to allow sensitive detection of various targets in colorimetric sensor platforms.[12,13] Single-atom nanozymes can exhibit higher catalytic efficiency and selectivity due to maximized atom utilization.[14,15] In this context, nanozymes exhibit immense potential for applications in biosensing, bioimaging, and therapeutic interventions for various diseases.[4–6,16–18] Therefore, studies have focused on developing diverse nanozymes, including those based on metal oxides, metal nanoparticles, carbon dots, and ferritin, all of which exhibit high enzyme-like activities.[4,6,17,19–21]

Fe_3O_4 nanoparticles have demonstrated intrinsic enzyme-mimetic activities similar to those of natural peroxidases despite being traditionally regarded as biologically and chemically inert.[16,17,22–26] In biomedical applications, iron oxide nanoparticles are used as sensor probes or therapeutic agents to catalyze the decomposition of H_2O_2 into highly reactive hydroxyl radicals or scavenge reactive oxygen species (ROS).[27,28] Efforts to enhance the catalytic performance of iron oxides have focused on the formation of complexes with carbon-based materials or other oxides, resulting in improved enzyme-like activities across diverse pH levels.[19,21,29,30] The peroxidase-like

Department of Chemical and Biological Engineering, Hanbat National University, Daejeon 34158, Korea. E-mail: jisil.choi@hanbat.ac.kr

† Electronic supplementary information (ESI) available: Material characterizations including zeta potential, TGA, XRD, and XPS of IOCs and enzymatic activity of IOC_400 and HRP with different concentration. See DOI: https://doi.org/10.1039/d5ra00047e

activity of bare Fe_3O_4 nanoparticles is attributed to their exposed surfaces, enabling efficient catalytic degradation of microplastics and facilitating easy recovery of the Fe_3O_4 surface coating.[31,32] In addition, the catalytic efficacy of iron oxide is influenced by its exposed facets, with particles exhibiting highly exposed [110] facets demonstrating a superior enzymatic activity.[33–35] The incorporation of Co into Fe_3O_4 NPs has been explored to enhance the multi-enzymatic activity of nanozymes and improve their therapeutic efficacy.[36] In terms of nanoparticle size, smaller nanoparticles have been reported to exhibit enhanced enzymatic activities.[22,37,38] Among the various shapes of Fe_3O_4 nanoparticles, including nanoclusters, nanoflowers, nanodiamonds, octahedral or triangular plates, and dodecahedral shapes, cluster spheres exhibit exceptional peroxidase-like activity.[33–35] Nonetheless, further research is required to elucidate the factors influencing the enzymatic properties of nanozymes, thereby expanding their potential applications in various fields. Specifically, although iron oxide nanoclusters (IOCs) have demonstrated superior enzymatic activity, the factors that enhance their activity remain unexplored. Thus, future investigations should focus on optimizing the performance of IOCs as nanozymes, thereby unlocking their full potential for diverse applications.

In this study, we investigated the size-dependent enzyme-like activities of IOCs. By examining the factors contributing to size dependency, we elucidated the advantages conferred by the clustered structure in enhancing enzymatic performance. Furthermore, we compared the enzymatic activity of IOCs to that of natural enzymes, such as horseradish peroxidase (HRP), under various environments to reveal their advantages over natural enzymes. Moreover, the optimized IOCs were proven to be efficient as colorimetric probes for glucose detection applications. This investigation provides essential insights into the structural advantages that influence enzyme-like properties and paves the way for the development of commercially available probes capable of replacing natural enzymes.

Experimental section

Reagents

All the reagents are listed below and were used as received without any purification: iron(III) chloride hexahydrate (97%, Sigma-Aldrich), ethylene glycol (99.5%, Samchun), sodium hydroxide (Duksan), anhydrous sodium acetate (NaOAc, Duksan), PAA (M.W.: 2000, 50% aqueous solution, Across Organics), sodium citrate dihydrate (99.0%, Daejung), anhydrous citric acid (99.5%, Samchun), anhydrous sodium phosphate dibasic (99.0%, Samchun), sodium bicarbonate (99.5%, Duksan), anhydrous sodium carbonate (99.0%, Samchun), hydrogen peroxide (34.5%, Samchun), TMB (TCI), HRP (Sigma-Aldrich), anhydrous dimethyl sulfoxide (99.8+%, Alfa Aesar), anhydrous dextrose (99.5%, Samchun), and glucose oxidase (GOx) from *Aspergillus niger* (Type VII, Sigma-Aldrich).

Equipment

The size of IOCs was analyzed *via* Cold Type FE-SEM (S-4800, Hitachi High Technology, Japan) and FE-TEM (200 kV Cs, HITACHI HF5000, Hitachi High Technology, Japan). The hydrodynamic sizes and surface charges of IOCs were measured using a Zetasizer (ZSU3200; Malvern Panalytical, UK). XRD (SmartLab, Rigaku, Japan) analyses were performed to determine the crystal structures of IOCs. The absorbance of IOCs was measured using a plate reader (Multimode Microplate Reader, SpectraMax M2e, Molecular Devices). XPS (K-Alpha+, Thermo Fisher Scientific, Waltham, MA, USA) was used to analyze the oxidation states of IOCs. The quantity of polymer coating of IOCs was determined *via* TGA (TGA-DSC 1 STARe, Mettler-Toledo, heating rate: 10 °C min^{-1}, atmosphere: nitrogen gas). The specific surface areas of IOCs were measured using the BET theory (BELSORP-miniII, BEL Japan, Inc).

Synthesis of IOCs

IOCs were synthesized *via* a modified solvothermal method described in our previous work.[30,32] For the synthesis of IOCs_30, 100, and 200, $FeCl_3 \cdot 6H_2O$ (0.68 g), PAA (0.293 g), NaOH, NaOAc, and EG (10 mL) were mixed and heated to 160 °C for 30 min, followed by maintenance at 160 °C for 1 h under an inert atmosphere. NaOH : NaOAc was added in ratios of 1 : 2, 1 : 5, and 0 : 1 to IOCs 30, 100, and 200, respectively. The reactants were then transferred to a solvent-heated reactor and allowed to react at 200 °C using an autoclave for 10 h. The resulting mixture was dissolved in water and was separated by removing the supernatant after centrifugation and acetone addition. IOC_400 was obtained under similar synthetic conditions as IOC_200, with the addition of more PAA (0.586 g) and EG (30 mL).

Peroxidase-like activity of IOCs

The peroxidase-like activity of IOCs was measured using TMB as the substrate. IOCs (30 μg Fe per mL) and H_2O_2 (100 mM) were added to a buffer solution (citrate buffer, pH 4, 10 mM), following the addition of TMB (3.12 mM). The absorbance of the resulting solution was measured at 652 nm. The enzymatic activity of IOCs was compared to that of HRP under various pH values from 2.0 to 8.0, H_2O_2 concentrations (0.1–300 mM), and temperatures (40, 50, and 70 °C).

Kinetic analysis

Kinetic analyses of IOCs and HRP were performed using TMB and H_2O_2 as substrates. IOCs (30 μg Fe per mL) or HRP (1 ng mL^{-1}) were added to a buffer solution (citrate buffer, pH 4, 10 mM). When H_2O_2 was used as the substrate, IOCs or HRP were added at concentrations ranging between 2.5–400 and 0.2–7.5 mM, respectively, followed by the rapid addition of TMB (3.12 mM). When TMB was used as the substrate, 100 mM H_2O_2 was used for IOCs, whereas 10 mM H_2O_2 was used for HRP, followed by rapid addition of 0.5–6 mM TMB. The absorbance of the resulting solution was measured at 652 nm.

The apparent kinetic parameters were calculated using the Michaelis–Menten equation, eqn (1).

$$V = \frac{([S]V_{max})}{([S] + K_m)} \quad (1)$$

where V is the initial velocity, V_{max} is the maximum reaction velocity, [S] is the substrate concentration, and K_m is the Michaelis constant. The Lineweaver–Burk plot, which is the linear regression curve of the relationship between $1/V$ and $1/[S]$, can be obtained by inverting the Michaelis–Menten equation to eqn (2).

$$\frac{1}{V} = \frac{K_m}{V_{max}}\frac{1}{[S]} + \frac{1}{V_{max}} \quad (2)$$

In the plot of $1/V$ *vs.* $1/[S]$, the ordinate and abscissa intercepts represent the inverse of V_{max} and $-1/K_m$, respectively. The K_m and V_{max} values were estimated from the intercepts.

Detection of glucose using the colorimetric system

Glucose was detected *via* a colorimetric assay using IOCs as the detection probe. First, GOx (1 mg mL^{-1}) and glucose (0.05–4 mM) were mixed in a phosphate buffer (pH 7.4, 10 mM) and incubated at 37 °C for 30 min. The total volume of the reaction solution is 100 μL. Next, IOCs (100 μg Fe per mL) and the buffer solution (citrate buffer, pH 4, 10 mM) were added to an incubated solution. TMB (3.12 mM) was added rapidly, and the resulting solution reacted at 40 °C. The absorbance of the solution was measured at 652 nm.

Results and discussion

IOCs with four different sizes were synthesized using a solvothermal approach based on our previous work.[39] The solvothermal method was a well-known approach for mass production.[40,41] Polyacrylic acid (PAA) was introduced to facilitate the entanglement of individual nanoparticles, promoting cluster formation while stabilizing the nanoparticle surfaces, resulting in IOCs with negative surface charges in pH 3 to 8 (Fig. S1†). The size of each IOC was determined to be 22.9, 118.1, 197.7, and 387.3 nm based on SEM analysis, indicating samples IOC_30, 100, 200, and 400, respectively (Fig. 1a–d). The hydrodynamic sizes of IOC_30, 100, 200, and 400 are 59.52, 92.89, 197.6, and 267.2 nm, respectively (Fig. S2†). The hydrodynamic sizes of IOCs closely match the sizes observed in SEM, indicating their stable dispersion in aqueous solution without aggregation. PAA content in IOCs was quantified *via* thermogravimetric analysis (TGA), revealing a consistent value of 15 wt% for all IOCs, except for IOC_30, which exhibited the smallest PAA proportion (5 wt%, Fig. S3†). Sharp X-ray diffraction (XRD) peaks indicated a crystalline magnetite structure (Fig. S4†). Furthermore, X-ray photoelectron spectroscopy (XPS) revealed that IOCs contained both Fe^{2+} and Fe^{3+} ions, confirming a magnetite structure (Fig. S5†). Therefore, IOCs of various sizes were successfully obtained.

The activities of IOCs of various sizes were investigated to evaluate the factors influencing the enzymatic effects of IOCs. All IOCs were examined for their enzymatic activity at the same concentration *via* mixing with 3,3′,5,5′-tetramethylbenzidine (TMB), and H_2O_2, and the color changes of the reaction solution were observed (Fig. 2a and b). As the particle size increased, the color changed to blue and became more pronounced. According to the changes in absorption at 652 nm over time, IOC_400

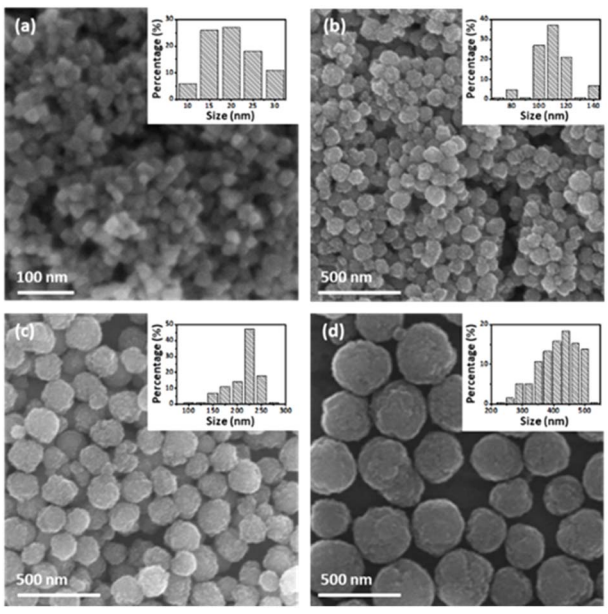

Fig. 1 SEM images of (a) IOC_30, (b) IOC_100, (c) IOC_200, and (d) IOC_400.

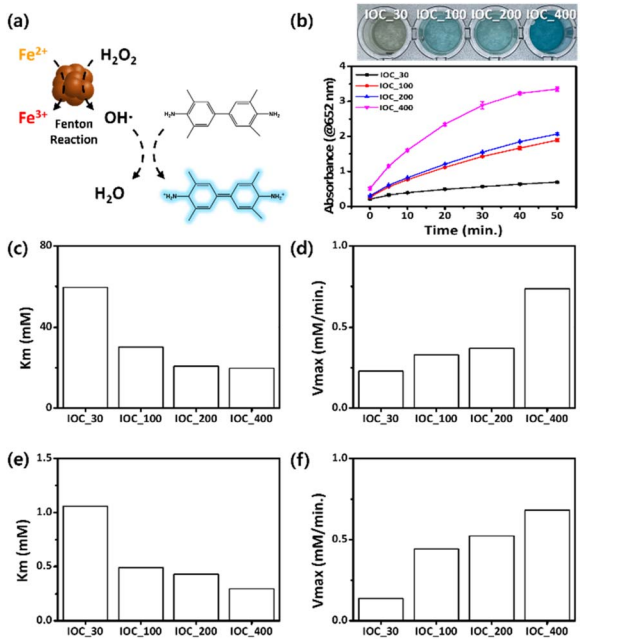

Fig. 2 (a) Schematic of the color changes through TMB oxidation by IOC. (b) IOC size-dependent color changes at 5 min and absorption intensities at 652 nm for an indicator solution containing IOCs (30 μg Fe per mL), H_2O_2 (100 mM), TMB (3.12 mM) and pH4 buffer solution at room temperature. K_m and V_{max} values were obtained using (c and d) H_2O_2 and (e and f) TMB as a substrate, respectively.

exhibited the most significant increase among the tested IOCs (Fig. 2b). The enzymatic effects of IOCs were further assessed by comparing their K_m and V_{max} values using H_2O_2 and TMB as substrates (Table S1†). In both cases, larger nanoclusters displayed lower K_m and higher V_{max} values, indicating a stronger enzymatic effect (Fig. 2c–f). The IOC exhibits a higher K_{cat}, defined based on the number of particles, compared to other reported Fe_3O_4-based nanozymes. In addition, IOCs showed higher enzymatic activity compared to single-core iron oxide nanoparticles with a diameter of 5 nm (SIO) (Fig. S6†). Additionally, larger nanoclusters exhibited higher K_{cat} values in both cases, indicating stronger enzymatic efficiency (Table S1†). Contrary to the common notion that smaller nanoparticles have higher enzyme-mimetic effects, our study revealed different observations.[22,33,34,37]

We hypothesized that the higher enzymatic properties of larger nanoclusters can be attributed to: (a) a higher ratio of oxidizable Fe^{2+} ions within the nanoclusters, and (b) an increased surface area. The surface coating ligand of IOCs, PAA, does not contribute to their enzymatic activity (Fig. S7†) and their different portion in IOCs (Fig. S3†) may not be a factor for their enzyme activity. First, the Fe^{2+} to Fe^{3+} ratio of each IOC was determined by measuring the peak area of each component *via* X-ray photoelectron spectroscopy (XPS). All IOCs comprised a similar ratio of ferrous ions among the total iron ions (approximately 30–35%), which is consistent with the ratio of Fe_3O_4 (Fig. S5e†). Therefore, the ratio of Fe^{2+} over Fe^{3+} in IOCs does not explain their size-dependent phenomena. Next, the surface area of IOCs was determined *via* Brunauer–Emmett–Teller (BET) measurements (Fig. 3a). Interestingly, the larger the IOC, the higher its specific surface area; IOC_400 exhibited the highest specific surface area. In addition, the size of the unit grains in IOCs was determined by the full width at half maximum (FWHM) of the XRD peaks, supporting the size-dependent surface area (Fig. 3b). The grain sizes of IOC_30, 100, 200, and 400 were calculated as 12, 9, 7, and 5 nm, respectively, using the Debye–Scherrer equation and considering the half-width maximum of the XRD peak. The grain sizes of individual unit nanoparticles were assessed *via* high-resolution transmission electron microscopy (HRTEM). The sizes of unit nanoparticles at the edge were measured as 9, 6, and 4 nm for IOCs_100, 200, and 400, respectively (Fig. 3c–f), which is similar to that determined based on FWHM of the XRD peaks (Fig. S4†). In the case of IOC_30, the individual grains were difficult to define in the HRTEM images because all the unit nanoparticles were attached as single crystals through oriented attachment. Therefore, the high activity of IOC_400 originates from the large specific surface area owing to the smaller grain size of the unit nanoparticles.

This observation aligns with the LaMer theory, stating that a weak basic environment results in slower nucleation and particle growth rates (Fig. 4a).[42–44] The hydroxide ions from the base present in the reaction accelerate the formation and growth of iron oxide nuclei nanoparticles, leading the size of unit particles to increase. Conversely, the unit particle size decreased for IOCs_30, 100, and 200, which were obtained by increasing the ratio of NaOAc over NaOH. In the case of IOC_400, synthesis involved the addition of a larger amount of

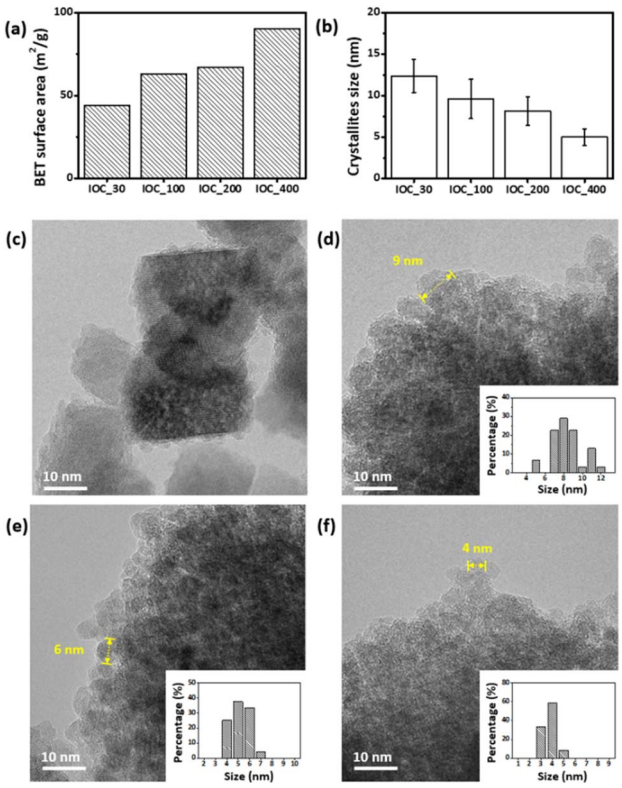

Fig. 3 (a) Surface area of IOC by size as measured *via* BET. (b) Grain size of IOC calculated using the Scherrer equation based on FWHM of the XRD peaks. TEM image of grains of (c) IOC_30, (d) IOC_100, (e) IOC_200, and (f) IOC_400.

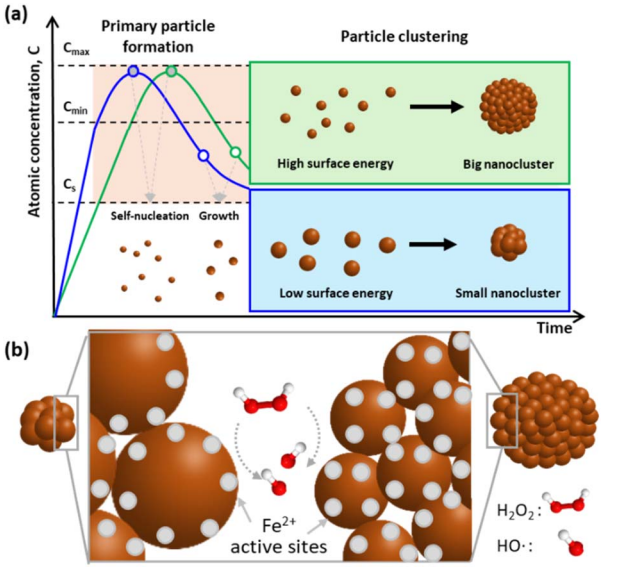

Fig. 4 (a) Schematics of IOCs formation. The size of primary particles are governed by precursor formation velocity and determines the size of whole size of IOCs. (b) Schematics of the active sites of ICOs with different size of primary particles.

EG (*i.e.*, solvent) and PAA compared to IOC_200. The diluted conditions of the iron source and alkali slowed down the conversion of the iron source to the precursors, resulting in the formation of small unit particles in IOC_400.[39,45,46] The presence of PAA impeded particle growth at a certain stage and induced particle clustering.[47] The concentration of PAA remained relatively consistent in all reactions, ensuring continued particle clustering even with IOC_400. During the clustering stage, the increased surface energy of the smaller nanoparticles facilitated rapid expansion and the formation of larger clusters (Fig. 4a).[47–49] As reported in previous studies,[50] IOCs possessed regions with oriented attachment at their core because of their densely packed structure. However, isolated unit nanoparticles are dispersed on the surface of IOCs, which can directly expose them to various substrates. Given that the overall size of IOCs increases with the presence of smaller unit nanoparticles, the formation of these unit nanoparticles is crucial in determining the IOC size and their enzymatic activity (Fig. 4b). Small-size unit nanoparticles can provide more active sites for the generation of hydroxyl radicals by decomposing hydrogen peroxide.[51] These findings elucidate the nuanced dynamics governing nanocrystal growth and provide valuable insights for tailoring IOC properties.

To assess their potential as substitutes for natural enzymes, the activity of IOC_400, which exhibited the highest enzymatic activity among IOCs, was compared with that of HRP under various conditions. IOC_400 exhibited a linear increase in absorbance with increasing concentration, and a noticeable blue color was visible to the naked eye from a concentration of 30 μg mL^{-1}. In comparison, HRP showed a deep blue color and high activity even at a low concentration of 1 ng mL^{-1} (Fig. S8†). In most studies, experiments are conducted based on the concentration that shows the highest activity or where saturation begins.[52–55] The concentrations of IOC_400 and HPR were determined to be 30 μg mL^{-1} and 1 ng mL^{-1}, respectively, based on their enzymatic activity at each concentration. Regarding the affinity to substrates, IOC demonstrated a lower affinity for H_2O_2 than HRP, whereas it exhibited a higher affinity for TMB than HRP (Fig. 5a and b). The initial velocities of each material were similar; however, their acceleration rates differed slightly depending on the substrate (Fig. 5b). HRP exhibited a higher enzymatic activity owing to its superior affinity for H_2O_2. K_{cat} was calculated using each V_{max} and the concentration of IOC or HRP (Table S1†).[16] The K_{cat} of IOC_400 is higher than that of HRP when H_2O_2 and TMB are used as substrates (Table S1†). While HRP has a single reaction pocket containing Fe ions,[17,51,56] a single IOC particle contains multiple active Fe ions.[51,56] Therefore, the enzyme activity based on whole IOC particles as a unit overwhelms that of HRPs although Fe ion-based enzyme activity of IOCs seems lower than that of HRPs. IOCs not only exhibit higher activity than natural enzymes but also offer significant advantages in terms of cost-effectiveness and stability. It is noteworthy that the enzymatic activity of IOC increased with H_2O_2 concentration, whereas that of HRP decreased after a rapid increase in H_2O_2 concentration (Fig. 5c and d). The low activity of HRP at high H_2O_2 concentrations was attributed to the competitive formation of an inactive

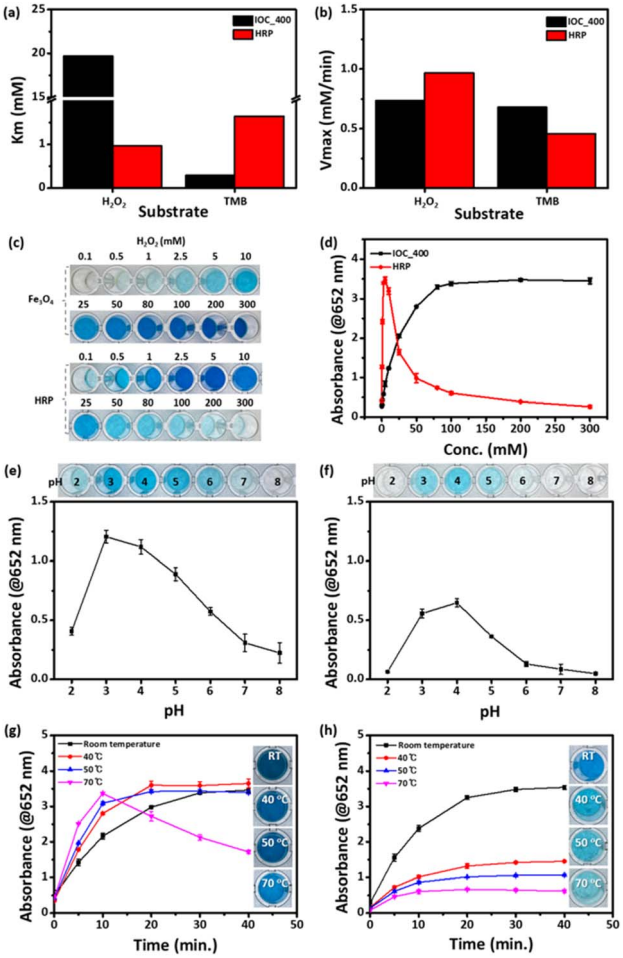

Fig. 5 (a) K_m and (b) V_{max} values of IOC_400 and HRP obtained using H_2O_2 and TMB as a substrate. (c) H_2O_2 concentration-dependent color changes and (d) absorption intensities at 652 nm at 30 min at room temperature. pH-dependent color changes at 5 min and absorption intensities at 652 nm of (e) IOC_400 and (f) HRP at room temperature. Temperature-dependent color changes and absorption intensities at 652 nm of (g) IOC_400 and (h) HRP at 10 min. All indicator solution containing IOCs (30 μg Fe per mL) or HRP (1 ng mL^{-1}), TMB (3.12 mM), and pH 4 buffer solution. pH and temperature-dependent color changes for an indicator solution containing 100 mM or 10 mM H_2O_2.

complex.[57–59] In contrast, IOCs do not possess the inactivation pathway, so their activity was not limited by H_2O_2 concentration. The activities of the two materials were also examined under various pH conditions from 2 to 8. IOCs exhibited enzymatic activity over a wider pH range of 2–6, whereas HRP exhibited activity in the pH range of 3–5 (Fig. 4e and f). The thermostability of the enzyme was also examined by investigating the effect of temperature on its activity. A significant decrease in HRP activity was observed over 40 °C, whereas IOC maintained its activity even over 70 °C (Fig. 5g and h). When IOCs were dispersed in an aqueous solution and stored under ambient conditions, their activity remained for at least 3 months (Fig. S9†). In addition, regardless of the synthetic batch, IOCs exhibited consistent enzyme activity (Fig. S10†). Therefore, IOC demonstrated stable enzymatic activity under a wide range

of H_2O_2 concentrations, pH, and temperatures compared to HRP, highlighting its versatility as a detection probe under harsh conditions.

The potential of IOC_400 as a detection probe was examined by employing IOC_400 for glucose detection. According to the World Health Organization, the global diabetic population continues to increase annually; therefore, novel glucose detection techniques are needed. While various diagnostic techniques exist, such as liquid chromatography-mass spectrometry, high-performance liquid chromatography, heart rate measurements, and electrochemical methods, they present challenges such as high costs, significant power demands, and the requirement for specialized equipment.[60,61] Our study highlights the potential of IOCs to detect glucose levels, being promising for the care of diabetic patients. In our experimental setup, glucose underwent oxidation to gluconic acid *via* glucose oxidase (GOx), resulting in the production of H_2O_2. Within the detection solution, IOC catalyzes the oxidation of TMB with generated H_2O_2 *via* GOx, inducing a color change to blue, thus enabling glucose detection (Fig. 6a). The intensity of this blue color correlates with the concentration of glucose due to the H_2O_2 concentration being directly proportional to the glucose concentration. The gold standard for the diagnosis of diabetes involves the measurement of blood glucose levels, where a fasting blood glucose level of ≥126 mg dL^{-1} (6.99 mM) indicates a disorder.[62] The blood sample is diluted by adding indication solution including H_2O_2, TMB, and buffer solution so that glucose solution with 6.99 mM is diluted to 1.17 mM in the test solution. Therefore, we conducted experiments within the final glucose concentration range of up to 4 mM in the assay solution, considering the dilution factors (Fig. 6b). The color change in the indicator solution occurred within 5 min of mixing and exhibited distinct alterations with increasing glucose concentrations. The plot of the absorption variation *vs.* glucose concentration exhibits a linear increase in the absorption intensity within the range of 0.1 to 4 mM of glucose. The limit of detection (LOD) and quantification (LOQ) is calculated to be 0.252 mM and 0.763 mM, respectively (Table S2†). Although the IOC still exhibits a relatively low LOD compared to other studies, it is evident that colorimetric readings can be significantly influenced by assay conditions or volume (*e.g.*, the length of the light source penetration path). In this study, minimal sample volumes (17 μL, total assay volume 100 μL) were used for detection, which can enhance patient comfort. Furthermore, considering the dilution of blood samples in the indicator solution, IOCs provided accurate glucose concentration information, demonstrating significant potential for streamlined diabetic care.

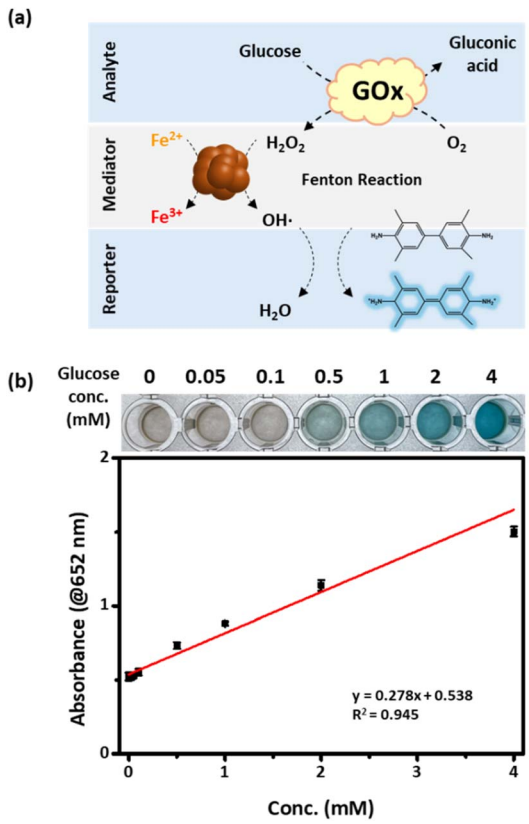

Fig. 6 (a) Schematic of glucose detection using the IOC nanozyme. (b) Glucose concentration-dependent color changes and absorption intensities at 652 nm at 5 min for an indicator solution containing TMB (3.12 mM), IOC_400 (100 μg Fe per mL), and GOx at room temperature.

Conclusions

In this study, we aimed to reveal the fundamental enzymatic activity of the IOC system and its potential as a colorimetric sensor. The enzymatic process of IOC is intricately linked to the size of its constituent nanoparticles, which enhance surface area based on unit particle size rather than the overall size of the nanoclusters. This remarkable enzymatic capability makes IOC highly efficient for glucose detection, a pivotal aspect of diabetes treatment. IOC, as a nanozyme, offers several advantages over natural enzymes, including enhanced durability, cost-effectiveness, and scalability for mass production. This study demonstrated IOC's potential for glucose detection. While the detection limit is relatively low, it meets diagnostic criteria for diseases, enabling effective detection even with small sample volumes. Additionally, IOC contains multiple active sites within a single particle unit, contributing to a high K_{cat} value. This implies that even with a single probe, IOC can deliver strong signals in detection systems such as ELISA. Moreover, the intrinsic separation capability of iron oxide can provide an additional advantage, synergistically improving targeted detection by eliminating undesired residues and concentrating probes. Functionalization with reactive groups (*e.g.*, DNA, peptides, antibodies) or structures (*e.g.*, molecularly imprinted polymers, MIPs) can further enhance target selectivity. Consequently, IOC shows promise for broader applications, particularly in strengthening detection capabilities for point-of-care testing.

Data availability

The authors confirm that the data supporting the findings of this study are available within the article and its ESI.†

Author contributions

Conceptualization, data curation, funding acquisition investigation methodology, project administration, supervision: JC. Writing – original draft, review & editing, formal analysis, validation, visualization: DB, MK, JC.

Conflicts of interest

There are no conflicts to declare.

Acknowledgements

This work was supported by National Research Foundation of Korea (NRF) grants funded by the Korean government (2020R1A5A8017671 and 2023R1A2C1005091).

References

1 M. Kohri, *Polym. J.*, 2014, **46**, 373–380.
2 K. Chattopadhyay and S. Mazumdar, *Biochemistry*, 1999, **39**, 263–270.
3 Y. Ouyang, M. P. O'Hagan and I. Willner, *Biosens. Bioelectron.*, 2022, **218**, 114768.
4 M. Zandieh and J. Liu, *Adv. Mater.*, 2023, **36**, 2211041.
5 M. Bilal, N. Khaliq, M. Ashraf, N. Hussain, Z. Baqar, J. Zdarta, T. Jesionowski and H. M. N. Iqbal, *Colloids Surf., B*, 2023, **221**, 112950.
6 B. Jiang, L. Fang, K. Wu, X. Yan and K. Fan, *Theranostics*, 2020, **10**, 687–706.
7 S. Shahraki, E. Vaziri, A. A. Saboury and K. Fan, *Coord. Chem. Rev.*, 2024, **517**, 215937.
8 H. Zhu, P. Liu, L. Xu, X. Li, P. Hu, B. Liu, J. Pan, F. Yang and X. Niu, *Biosens*, 2021, **11**, 382.
9 R. G. Mahmudunnabi, F. Z. Farhana, N. Kashaninejad, S. H. Firoz, Y.-B. Shim and M. J. A. Shiddiky, *Analyst*, 2020, **145**, 4398–4420.
10 F. Zhao, L. Wang, M. Li, M. Wang, G. Liu and J. Ping, *TrAC, Trends Anal. Chem.*, 2023, **165**, 117152.
11 C. Li, T. Hang and Y. Jin, *Exploration*, 2023, **3**, 20220151.
12 W. Liu, L. Chu, C. Zhang, P. Ni, Y. Jiang, B. Wang, Y. Lu and C. Chen, *Chem. Eng. J.*, 2021, **415**, 128876.
13 A. Lee, W. Kang and J. Choi, *Nanomaterials*, 2021, **11**, 3046.
14 S. Zhang and X.-D. Zhang, *Nano Biomed. Eng.*, 2024, **16**, 1–27.
15 I. Zare, D. Choi, J. Zhang, M. T. Yaraki, A. Ghaee, S. Z. Nasab, R. Taheri-Ledari, A. Maleki, A. Rahi, K. Fan and J. Lee, *Nano Today*, 2024, **56**, 102276.
16 A. D. Bokare and W. Choi, *J. Hazard. Mater.*, 2014, **275**, 121–135.
17 L. Gao, K. Fan and X. Yan, *Theranostics*, 2017, **7**, 3207–3227.
18 Y. Zhong, X. Tang, J. Li, Q. Lan, L. Min, C. Ren, X. Hu, R. M. Torrente-Rodríguez, W. Gao and Z. Yang, *Chem. Commun.*, 2018, **54**, 13813–13816.
19 M. Li, Y.-H. Lao, R. L. Mintz, Z. Chen, D. Shao, H. Hu, H.-X. Wang, Y. Tao and K. W. Leong, *Nanoscale*, 2019, **11**, 2631–2636.
20 N. Alizadeh, A. Salimi, R. Hallaj, F. Fathi and F. Soleimani, *Mater. Sci. Eng., C*, 2019, **99**, 1374–1383.
21 L. Xu and J. Wang, *Environ. Sci. Technol.*, 2012, **46**, 10145–10153.
22 L. Gao, J. Zhuang, L. Nie, J. Zhang, Y. Zhang, N. Gu, T. Wang, J. Feng, D. Yang, S. Perrett and X. Yan, *Nat. Nanotechnol.*, 2007, **2**, 577–583.
23 H. Wei and E. Wang, *Anal. Chem.*, 2008, **80**, 2250–2254.
24 X. Yuan, S. Cheng, L. Chen, Z. Cheng, J. Liu, H. Zhang, J. Yang and Y. Li, *Talanta*, 2023, **258**, 124407.
25 N. V. S. Vallabani and S. Singh, *3 Biotech*, 2018, **8**, 279.
26 S. Guo and L. Guo, *J. Phys. Chem. C*, 2019, **123**, 30318–30334.
27 Z. Du, Y. Wang, D. He, E. Xu, Q. Chai, Z. Jin, Z. Wu and B. Cui, *Food Chem.*, 2022, **397**, 133756.
28 Q. Zhu, Y. Huang, X. Zhu, L. Peng, H. Wang, S. Gao, Z. Yang, J. Zhang and X. Liu, *Mater. Today Bio*, 2023, **19**, 100568.
29 Y. Zheng, D. Xu, L. Sun, J. Ji, J. Sun, Z. Tong, L. Qin, Y. Zhang, J. Luo and D. Liao, *Colloids Surf., A*, 2022, **648**, 129046.
30 N. Luo, Z. Yang, F. Tang, D. Wang, M. Feng, X. Liao and X. Yang, *ACS Appl. Nano Mater.*, 2019, **2**, 3951–3959.
31 M. Zandieh and J. Liu, *Angew. Chem., Int. Ed.*, 2022, **61**, e202212013.
32 F. Yu, Y. Huang, A. J. Cole and V. C. Yang, *Biomaterials*, 2009, **30**, 4716–4722.
33 S. Fu, S. Wang, X. Zhang, A. Qi, Z. Liu, X. Yu, C. Chen and L. Li, *Colloids Surf., B*, 2017, **154**, 239–245.
34 S. Liu, F. Lu, R. Xing and J. Zhu, *Chem. - Eur. J.*, 2010, **17**, 620–625.
35 X.-L. Cheng, J.-S. Jiang, D.-M. Jiang and Z.-J. Zhao, *J. Phys. Chem. C*, 2014, **118**, 12588–12598.
36 J. Chang, X. Qin, S. Li, F. He, S. Gai, H. Ding and P. Yang, *ACS Appl. Mater. Interfaces*, 2022, **14**, 45217–45228.
37 F. F. Peng, Y. Zhang and N. Gu, *Chin. Chem. Lett.*, 2008, **19**, 730–733.
38 S. Wu, D. Guo, X. Xu, J. Pan and X. Niu, *Sens. Actuators, B*, 2020, **303**, 127225.
39 S. Lee, A. Byun and J. Choi, *J. Powder Mater.*, 2023, **30**, 297–304.
40 K. M. Ø. Jensen, H. L. Andersen, C. Tyrsted, E. D. Bøjesen, A.-C. Dippel, N. Lock, S. J. L. Billinge, B. B. Iversen and M. Christensen, *ACS Nano*, 2014, **8**, 10704–10714.
41 C. Xu and A. S. Teja, *J. Supercrit. Fluids*, 2008, **44**, 85–91.
42 J. Liang, H. Ma, W. Luo and S. Wang, *Mater. Chem. Phys.*, 2013, **139**, 383–388.
43 S. Xuan, Y.-X. J. Wang, J. C. Yu and K. Cham-Fai Leung, *Chem. Mater.*, 2009, **21**, 5079–5087.
44 M. Zhu and G. Diao, *J. Phys. Chem. C*, 2011, **115**, 18923–18934.
45 H. Sharifi Dehsari, A. Halda Ribeiro, B. Ersöz, W. Tremel, G. Jakob and K. Asadi, *CrystEngComm*, 2017, **19**, 6694–6702.
46 H. Zeng, P. M. Rice, S. X. Wang and S. Sun, *J. Am. Chem. Soc.*, 2004, **126**, 11458–11459.
47 V. Ganesan, B. B. Lahiri, C. Louis, J. Philip and S. P. Damodaran, *J. Mol. Liq.*, 2019, **281**, 315–323.
48 J. Kim, V. T. Tran, S. Oh, C.-S. Kim, J. C. Hong, S. Kim, Y.-S. Joo, S. Mun, M.-H. Kim, J.-W. Jung, J. Lee, Y. S. Kang,

J.-W. Koo and J. Lee, *ACS Appl. Mater. Interfaces*, 2018, **10**, 41935–41946.
49 L. Zhuang, W. Zhang, Y. Zhao, H. Shen, H. Lin and J. Liang, *Sci. Rep.*, 2015, **5**, 9320.
50 M. Jeong, S. Lee, D. Y. Song, S. Kang, T.-H. Shin and J. Choi, *ACS Omega*, 2021, **6**, 31161–31167.
51 Y. Qiu, B. Yuan, H. Mi, J.-H. Lee, S.-W. Chou and Y.-K. Peng, *J. Phys. Chem. Lett.*, 2022, **13**, 8872–8878.
52 Y. Dong, H. Zhang, Z. U. Rahman, L. Su, X. Chen, J. Hu and X. Chen, *Nanoscale*, 2012, **4**, 3969.
53 M. K. Masud, J. Kim, Md. M. Billah, K. Wood, M. J. A. Shiddiky, N.-T. Nguyen, R. K. Parsapur, Y. V. Kaneti, A. A. Alshehri, Y. G. Alghamidi, K. A. Alzahrani, M. Adharvanachari, P. Selvam, Md. S. A. Hossain and Y. Yamauchi, *J. Mater. Chem. B*, 2019, **7**, 5412–5422.
54 R. Bhattacharjee, S. Tanaka, S. Moriam, M. K. Masud, J. Lin, S. M. Alshehri, T. Ahamad, R. R. Salunkhe, N.-T. Nguyen, Y. Yamauchi, Md. S. A. Hossain and M. J. A. Shiddiky, *J. Mater. Chem. B*, 2018, **6**, 4783–4791.
55 M. A. Wahab, S. M. A. Hossain, M. K. Masud, H. Park, A. Ashok, M. Mustapić, M. Kim, D. Patel, M. Shahbazi, Md. S. A. Hossain, Y. Yamauchi and Y. V. Kaneti, *Sens. Actuators, B*, 2022, **366**, 131980.
56 K. Wan, B. Jiang, T. Tan, H. Wang and M. Liang, *Small*, 2022, **18**, 2204372.
57 J. A. Nicell and H. Wright, *Enzyme Microb. Technol.*, 1997, **21**, 302–310.
58 M. B. Arnao, M. Acosta, J. A. del Rio, R. Varón and F. García-Cánovas, *Biochim. Biophys. Acta*, 1990, **1041**, 43–47.
59 P. George, *J. Biol. Chem.*, 1953, **201**, 427–434.
60 W. Villena Gonzales, A. Mobashsher and A. Abbosh, *Sensors*, 2019, **19**, 800.
61 M. L. Firdaus, E. Saputra, S. M. Ginting, S. Wyantuti, D. R. Eddy, L. Rahmidar and B. Yuliarto, *Sens. Bio-Sens. Res.*, 2022, **35**, 100472.
62 N. V. S. Vallabani, A. S. Karakoti and S. Singh, *Colloids Surf., B*, 2017, **153**, 52–60.